Crystalline topological Dirac semimetal phase in rutile structure β'-PtO_2

Rokyeon Kim,[1,2,*] Bohm-Jung Yang,[1,2,3] and Choong H. Kim[1,2,†]
[1]*Department of Physics and Astronomy, Seoul National University, Seoul 08826, Korea*
[2]*Center for Correlated Electron Systems, Institute for Basic Science, Seoul 08826, Korea*
[3]*Center for Theoretical Physics, Seoul National University, Seoul 08826, Korea*

(Received 22 September 2018; published 16 January 2019)

Based on first-principles calculations and symmetry analysis, we propose that a transition-metal rutile oxide, in particular β'-PtO_2, can host a three-dimensional topological Dirac semimetal phase. We find that β'-PtO_2 possesses an inner nodal chain structure when spin-orbit coupling is neglected. Incorporating spin-orbit coupling gaps the nodal chain while preserving a single pair of three-dimensional Dirac points protected by a screw rotation symmetry. These Dirac points are created by a band inversion of two d bands, which is a realization of a Dirac semimetal phase in a correlated electron system. Moreover, a mirror plane in the momentum space carries a nontrivial mirror Chern number $n_M = -2$, which distinguishes β'-PtO_2 from the Dirac semimetals known so far, such as Na_3Bi and Cd_3As_2. If we apply a perturbation that breaks the rotation symmetry and preserves the mirror symmetry, the Dirac points are gapped, and the system becomes a topological crystalline insulator.

DOI: 10.1103/PhysRevB.99.045130

I. INTRODUCTION

Three-dimensional (3D) Dirac semimetals (DSMs) are materials that are characterized by fourfold degenerate nodal points or lines. The low-energy excitations of DSMs describe Dirac fermions, and this direct correspondence to the elementary particle enables us to explore high-energy physics in condensed-matter systems. Especially, DSMs can carry nontrivial topological numbers, which lead to the observations of intriguing effects such as the surface Fermi arcs [1], giant magnetoresistance [2], and quantum oscillations [3].

Because of these unique properties, comprehensive theoretical studies were carried out on the existence and protection of Dirac points in materials. For the systems without spin-orbit coupling (SOC), inversion (P) and time-reversal (T) symmetries protect nodal lines owing to the quantized Berry phases [4,5]. When SOC is included, however, the nodal lines are gapped, and we require additional crystalline symmetries to protect Dirac points. The protection of Dirac points in the presence SOC can be classified into two cases, namely, the band inversion and the symmetry-enforced mechanisms. They can be explained in a unified way by inspecting the rotation symmetries of crystals [6]. When a crystal has a rotation symmetry (including a screw rotation), a pair of Dirac points can be protected on the rotation axis via the band inversion mechanism [7,8], whereas when a crystal has a screw rotation symmetry, a single Dirac point is enforced at the Brillouin zone boundary [9,10].

For the first case, when we choose the k_z axis as a rotation axis, the $k_z = 0$ or π plane can carry two-dimensional (2D) topological invariants [6]. For example, DSMs Na_3Bi [7] and Cd_3As_2 [8], which have been verified in experiments [11–14], are shown to have nontrivial $\mathbb{Z}_2$ invariants. While the theory also predicts a mirror Chern number $n_M = |2|$ (and $|3|$) [6], until recently, there have been no studies on the DSMs with a mirror Chern number $n_M = |2|$. A DSM carrying a nontrivial mirror Chern number, which we call a *crystalline* topological DSM, is topologically distinct from the conventional DSM possessing a nontrivial $\mathbb{Z}_2$ number protected by T symmetry. To our knowledge, only VAl_3 was proposed to be a type-II DSM that has a mirror Chern number $n_M = 2$ [15]. In contrast to a type-I DSM, where the Fermi surface shrinks to isolated points, a type-II DSM features the Fermi surface composed of electron and hole pockets, which is due to a tilted Dirac cone [16].

In this paper, we show that the rutile phase PtO_2, β'-PtO_2, is a type-I 3D topological DSM that possesses a nontrivial mirror Chern number $n_M = -2$. We carried out the density functional theory (DFT) calculations and symmetry analysis, which reveal the protection mechanism of the Dirac points and the topological nature of the system. Recently, a number of theoretical studies were performed on the topological phases of the rutile oxides with transition-metal ions. For example, the Chern insulating state [17] and the quantum spin Hall phase [18] were predicted in the rutile-based heterostructures. In addition, for the 3D bulks, IrO_2 was shown to have Dirac nodal lines on the zone boundary [19], and β-PbO_2 was proposed to be a 3D DSM [20,21].

Compared with the DSMs studied so far, the DSM phase of β'-PtO_2 shows distinct features. Unlike β-PbO_2 and other DMSs, which usually involve s and p bands, the DSM phase of β'-PtO_2 is realized in a correlated electron system by a band inversion of two d bands. Moreover, as the system carries a nontrivial mirror Chern number, 2D topological phases [17,18] as well as the topological crystalline insulator (TCI) phase can be achieved in β'-PtO_2 by reducing the dimension and breaking the symmetries. Therefore, the crystal structures based on β'-PtO_2 may serve as a platform to study the

*rrykim@gmail.com
†chkim82@snu.ac.kr

correlation effects and the various topological phases in DSMs. The possible influence of electronic correlations in DSMs includes the correlation-induced semimetal-insulator transitions [22–24] and unusual quantum critical transports [25–27]. Last, we point out that the mirror symmetry $M_z : z \to -z$ in the rutile structure was overlooked in Refs. [18,20,21], and they missed the correct description of 2D topological invariants, which we present in this study.

II. METHOD AND CRYSTAL STRUCTURE

To investigate the electronic structures of the transition-metal rutile oxides, we have carried out the DFT calculations using the Vienna *ab initio* simulation code [28]. The projector augmented-wave method [29] and the exchange-correlation functional of the generalized gradient approximation (GGA) in the Perdew, Burke, and Ernzerhof [30] scheme were used. To improve the estimation of a band gap, we further employed the Heyd-Scuseria-Ernzerhof (HSE) hybrid functional calculations [31]. The self-consistent total energy was evaluated with an $8 \times 8 \times 12$ k-point mesh, and the cutoff energy for the plane-wave basis set was 500 eV.

A transition-metal rutile oxide, MO_2, has a tetragonal structure with space group $P4_2/mnm$ (No. 136). This compound can contain group-VIII transition metals, such as Rh, Pd, Ir, and Pt. Especially, platinum dioxides can be crystallized in the rutile phase β'-PtO_2 [32] along with allotropes β-PtO_2 (space group $Pnnm$) [33] and α-PtO_2 (space group $P\bar{3}m1$) [34]. Although the calculated energy of β-PtO_2 is the lowest of the three, the energy differences between the structures are relatively small [35]. Experimentally, when high O_2 pressure in the range of 40 to 60 kbar is used, the rutile phase β'-PtO_2 can be stabilized among the three structures [32].

In the unit cell of the rutile structure, two cations, $M(1)$ and $M(2)$, are displaced by $\boldsymbol{\tau} = (\frac{1}{2}, \frac{1}{2}, \frac{1}{2})$ [in units of (a, a, c)] from one another, and each cation is surrounded by six oxygen atoms, as shown in Fig. 1(a). The space group includes five generators: E, C_{2z}, $\widetilde{C}_{4z} = \{C_{4z}|\boldsymbol{\tau}\}$, $\widetilde{C}_{2y} = \{C_{2y}|\boldsymbol{\tau}\}$, and P, where E is the identity, C_{2z} is a twofold rotation about the z axis, and $\widetilde{C}_{4z}$ ($\widetilde{C}_{2y}$) is a fourfold (twofold) rotation about the z axis (y axis), C_{4z} (C_{2y}), followed by a translation by $\boldsymbol{\tau}$. Among the 16 symmetry operations constructed from the generators, the following symmetries are important in this study:

$$P,\ \widetilde{C}_{4z},\ M_z = M_{[001]},\ M_{[110]},\ M_{[1\bar{1}0]},$$

where $M_{\mathbf{n}}$ is a mirror reflection about the plane defined by a normal vector $\mathbf{n}$. Additionally, as we focus on nonmagnetic systems, we include T symmetry.

III. RESULTS

Figures 1(c) and 1(d) show the GGA and GGA + SOC band structures, respectively, of β'-PtO_2 with the experimental lattice constants $a = 4.485$ Å, $c = 3.130$ Å [32]. Without SOC we have nodal points near the Fermi level on the M-Γ, Γ-Z, and A-Z lines [Fig. 1(c)]. As the Pt ion in the rutile structure has a $5d^6$ configuration and octahedral-like coordination, the nodal points are created by a band inversion of t_{2g} and e_g bands. When we include SOC, however, the nodal points

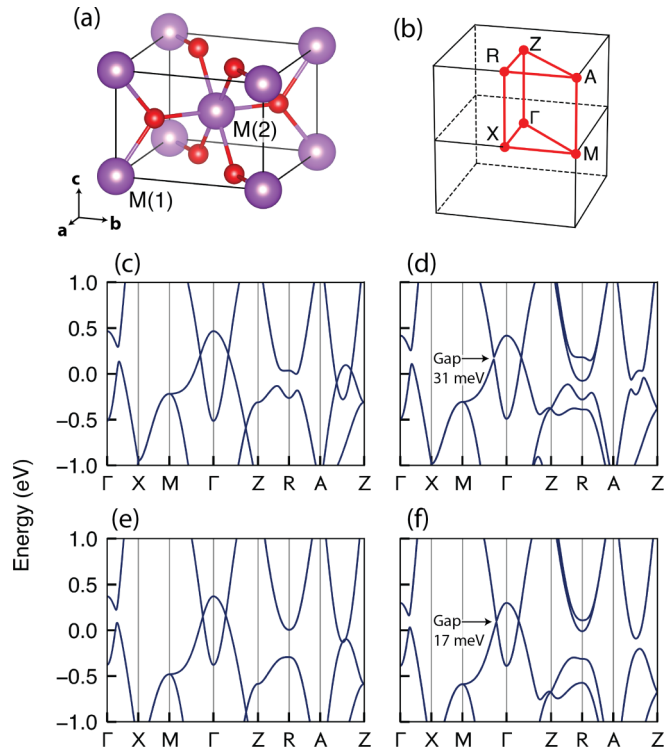

FIG. 1. (a) Crystal structure of the rutile oxides. (b) Tetragonal Brillouin zone. (c) GGA and (d) GGA + SOC band structures of β'-PtO_2. (e) GGA and (f) GGA + SOC band structures of β'-PtO_2 uniformly compressed by 3%.

are gapped, except for the ones on the Γ-Z line [Fig. 1(d)]. In other words, in the presence of SOC, we observe the 3D DSM phase of β'-PtO_2, which has a band gap locally at every $\mathbf{k}$ point except the Dirac points on the Γ-Z line. We note, however, that the Dirac points are slightly above the Fermi level because of the bands on the $k_z = \pi$ plane. Although the system can be utilized as a DSM in its present condition, we can additionally tune the band structure to move the Dirac points close to the Fermi level. We find that the bands on the $k_z = \pi$ plane can be removed by applying a uniform compressive strain. For example, when we apply a uniform compressive strain of 3%, the bands on the $k_z = \pi$ plane are pushed away, and the Dirac points get closer to the Fermi level, as we can see in the GGA [Fig. 1(e)] and GGA + SOC [Fig. 1(f)] band structures. Having revealed that β'-PtO_2 hosts a DSM phase, we investigate the protection mechanism of the Dirac points and the topological properties of the system in the subsequent sections.

A. Dirac nodal lines without SOC

We begin by reviewing the general properties of a band structure with symmetries. The presence of both P and T symmetries ensures that the band structure is symmetric in $\mathbf{k}$ and $-\mathbf{k}$ points and is doubly degenerate at every $\mathbf{k}$ point. In general, when we consider a symmetry operation $\widetilde{g} = \{g|\mathbf{t}\}$ of a system, the invariance of the system under $\widetilde{g}$ requires that the Bloch Hamiltonian satisfies $\widetilde{g}H(\mathbf{k})\widetilde{g}^{-1} = H(R_g\mathbf{k})$, where R_g is a rotation matrix representing g. As a result, for the $\mathbf{k}$

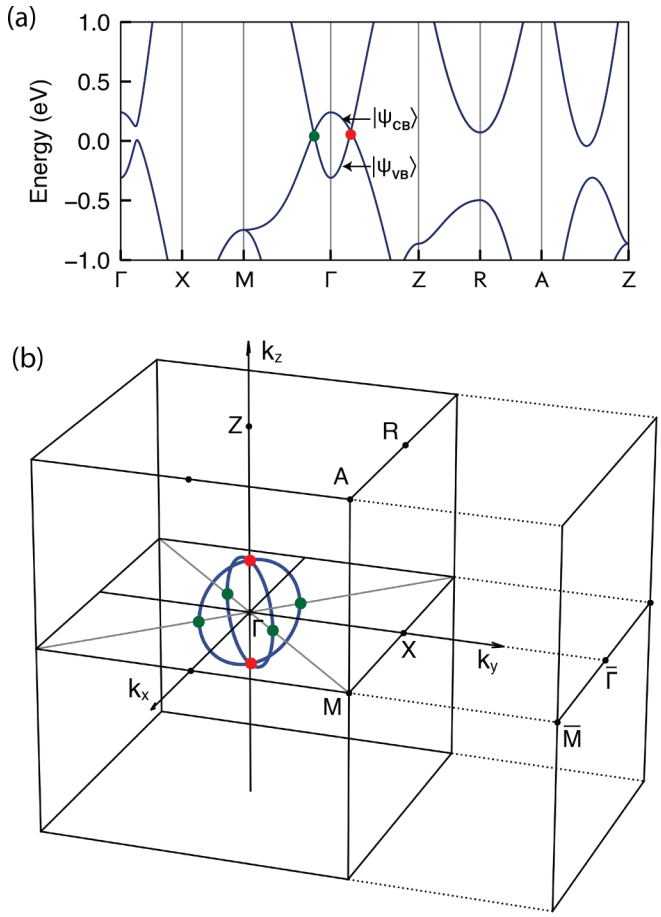

FIG. 2. (a) GGA band structure of β'-PtO_2 uniformly compressed by 5%. The valence band $|\psi_{VB}\rangle$ is in contact with the conduction band $|\psi_{CB}\rangle$ at the Dirac points (green and red dots). (b) Whole Dirac nodal line structure without SOC. Two ring-shaped nodal lines on the (110) and (1$\bar{1}$0) planes join at the two points on the k_z axis (red dots). The bulk Brillouin zone and the surface Brillouin zone projected on the (010) surface are shown.

point that is invariant under R_g, i.e., $R_g\mathbf{k} = \mathbf{k}$, $\tilde{g}$ and $H(\mathbf{k})$ commute, and a Bloch state can be labeled by a $\tilde{g}$ eigenvalue.

Figure 2(a) shows the band structure of β'-PtO_2 in the absence of SOC ($T^2 = 1$). Here, to focus on the band structure on the $k_z = 0$ plane and k_z axis, we apply a uniform compressive strain of 5% to the system, but we emphasize that the system shows a DSM phase even without any strain. In the band structure, we observe nodal points on the Γ-M and Γ-Z lines at $(k_0, k_0, 0)$ and $(0, 0, k_d)$, respectively, where $k_0 = 0.20\,\pi$ and $k_d = 0.23\,\pi$ [momenta are in units of $(\frac{1}{a}, \frac{1}{a}, \frac{1}{c})$]. In fact, the nodal points are parts of the nodal lines in the (110) and (1$\bar{1}$0) planes, as shown in Fig. 2(b). The whole nodal line structure exhibits two ring-shaped nodal lines in the (110) and (1$\bar{1}$0) planes that touch at $k_z = \pm k_d$.

To explain the nodal line structure, we first consider the screw rotation $\widetilde{C}_{4z}$. Under the successive operations of $\widetilde{C}_{4z}$ on the coordinates (x, y, z), we have $\widetilde{C}_{4z}^4 : (x, y, z) \to (x, y, z + 2)$. Thus, we can write $\widetilde{C}_{4z}^4 = \tau(0, 0, 2)$, where $\tau(\alpha, \beta, \gamma)$ $(\alpha, \beta, \gamma \in \mathbb{Z})$ is a translation operator. Since the effect of the translation operator acting on a Bloch state is $\tau(\alpha, \beta, \gamma)|\psi(\mathbf{k})\rangle = e^{-i(\alpha k_x + \beta k_y + \gamma k_z)}|\psi(\mathbf{k})\rangle$, we obtain

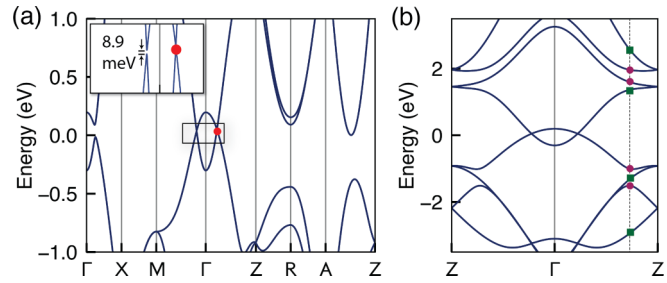

FIG. 3. (a) GGA + SOC band structure of β'-PtO_2 uniformly compressed by 5%. The Dirac nodal lines are gapped except for the Dirac points on the k_z axis (red dot). (b) Bands on the k_z axis are labeled by $\widetilde{C}_{4z}$ eigenvalues. Purple dots denote $\{\widetilde{c}_{4z}(0), \widetilde{c}_{4z}(3)\}$, and green squares denote $\{\widetilde{c}_{4z}(1), \widetilde{c}_{4z}(2)\}$.

$\widetilde{C}_{4z}^4 = e^{-i2k_z}$. As a result, for the Bloch states on the k_z axis, $\widetilde{C}_{4z}$ eigenvalues are given by $e^{-i\frac{k_z}{2}}e^{i\frac{\pi}{2}n}$ $(n = 0, 1, 2, 3)$.

For the band structure of β'-PtO_2, two bands near the Fermi level, which we denote $|\psi_{VB}\rangle$ and $|\psi_{CB}\rangle$ [see Fig. 2(a)], are mostly composed of the d_{xy} and $d_{x^2-y^2}$ orbitals, respectively. On the k_z axis, these bands can be written in the orbital basis as

$$|\psi_{VB}\rangle = \sum_{\mathbf{R}} e^{ik_zR_z}\left[|d_{xy}\rangle_{Pt(1)} + e^{i\frac{k_z}{2}}|d_{xy}\rangle_{Pt(2)}\right]_{\mathbf{R}},$$

$$|\psi_{CB}\rangle = \sum_{\mathbf{R}} e^{ik_zR_z}\left[|d_{x^2-y^2}\rangle_{Pt(1)} - e^{i\frac{k_z}{2}}|d_{x^2-y^2}\rangle_{Pt(2)}\right]_{\mathbf{R}},$$

where $\mathbf{R}$ is a lattice vector and other orbitals are omitted for simplicity. Because of the nonsymmorphic character of the $\widetilde{C}_{4z}$ symmetry, $|\psi_{VB}\rangle$ and $|\psi_{CB}\rangle$ have $\widetilde{C}_{4z}$ eigenvalues $-e^{-i\frac{k_z}{2}}$ and $+e^{-i\frac{k_z}{2}}$, respectively. As the two bands belong to the different eigenvalues, they can cross on the k_z axis without a hybridization and can form a pair of Dirac points at $k_z = \pm k_d$.

Next, we examine the mirror operations $M_{[110]}$ and $M_{[1\bar{1}0]}$. Since the (110) and (1$\bar{1}$0) planes are invariant under $M_{[110]}$ and $M_{[1\bar{1}0]}$, respectively, we can label the Bloch states on these planes with mirror eigenvalues. For each mirror plane, $|\psi_{VB}\rangle$ and $|\psi_{CB}\rangle$ have mirror eigenvalues $+1$ and -1, respectively; therefore, they can form a nodal line on the mirror plane. The two nodal lines on the (110) and (1$\bar{1}$0) planes have identical shapes because of the $\widetilde{C}_{4z}$ symmetry. Moreover, as the mirror planes contain the k_z axis, the nodal lines should pass through the points $(0, 0, +k_d)$ and $(0, 0, -k_d)$. Consequently, without SOC, we have an inner nodal chain structure [36,37], as shown in Fig. 2(b).

B. Protection of Dirac points with SOC

In the presence of SOC ($T^2 = -1$), the nodal lines in the mirror planes are gapped, as we can observe in the GGA + SOC band structure in Fig. 3(a). We can explain the instability of the nodal lines by inspecting the mirror eigenvalues of the bands with SOC. We first note that mirror eigenvalues take two imaginary values $\pm i$. In general, on a plane that is invariant under a mirror operation $M_{\mathbf{n}}$, a Bloch state $|\psi(\mathbf{k})\rangle$ and its degenerate partner $PT|\psi(\mathbf{k})\rangle$ have different mirror eigenvalues because of the commutation relations $[P, T] = [M_{\mathbf{n}}, T] = [P, M_{\mathbf{n}}] = 0$. Therefore, when two sets

of degenerate bands approach on the mirror plane, there is an unavoidable hybridization between them, and band gaps must open.

The Dirac points on the k_z axis, however, are protected even with SOC [see Fig. 3(a)], which is due to the $\widetilde{C}_{4z}$ symmetry. First, with SOC, we have $\widetilde{C}_{4z}^4 = e^{-i2k_z}(-1)$, where the value of -1 is from the 2π rotation of a half-integer spin. Therefore, $\widetilde{C}_{4z}$ eigenvalues take

$$\widetilde{c}_{4z}(n) = e^{-i\frac{k_z}{2}} e^{i\frac{\pi}{2}(n+\frac{1}{2})} \quad (n = 0, 1, 2, 3).$$

Next, because of the nonsymmorphic nature of $\widetilde{C}_{4z}$, we have the relation $\widetilde{C}_{4z}P = \tau(1,1,1)P\widetilde{C}_{4z}$ in addition to the commutation relations $[T, P] = [T, \widetilde{C}_{4z}] = 0$. Then, for a Bloch state $|\psi(\mathbf{k})\rangle$ on the k_z axis with a $\widetilde{C}_{4z}$ eigenvalue $e^{-i\frac{k_z}{2}} e^{i\frac{\pi}{2}(n+\frac{1}{2})}$, we have

$$\begin{aligned}\widetilde{C}_{4z}PT|\psi(\mathbf{k})\rangle &= T\tau(1,1,1)P\widetilde{C}_{4z}|\psi(\mathbf{k})\rangle \\ &= e^{-i\frac{k_z}{2}} e^{-i\frac{\pi}{2}(n+\frac{1}{2})} PT|\psi(\mathbf{k})\rangle.\end{aligned}$$

As a result, we find that a degenerate doublet $\{|\psi(\mathbf{k})\rangle, PT|\psi(\mathbf{k})\rangle\}$ of the Bloch Hamiltonian can have a pair of $\widetilde{C}_{4z}$ eigenvalues $\{\widetilde{c}_{4z}(0), \widetilde{c}_{4z}(3)\}$ or $\{\widetilde{c}_{4z}(1), \widetilde{c}_{4z}(2)\}$.

With $\widetilde{C}_{4z}$ eigenvalues of degenerate doublets, we can identify two classes of Dirac points on the k_z axis. First, if a doublet has $\widetilde{C}_{4z}$ eigenvalues $\{\widetilde{c}_{4z}(0), \widetilde{c}_{4z}(3)\}$, it should touch another doublet with $\{\widetilde{c}_{4z}(1), \widetilde{c}_{4z}(2)\}$ at the zone boundary $k_z = \pm\pi$ because of the connectivity conditions imposed on $\widetilde{c}_{4z}(n)$ [38]. Namely, two doublets whose four bands have all different $\widetilde{C}_{4z}$ eigenvalues stick together at the zone boundary. To be more specific, at the $k_z = \pm\pi$ point, four degenerate states $\{|\psi(\mathbf{k})\rangle, P|\psi(\mathbf{k})\rangle, T|\psi(\mathbf{k})\rangle, PT|\psi(\mathbf{k})\rangle\}$ can exhaust all $\widetilde{C}_{4z}$ eigenvalues because of the anticommutation relation $P\widetilde{C}_{4z} = -\widetilde{C}_{4z}P$ at this point. Thus, for the systems with $\widetilde{C}_{4z}$ symmetry, Dirac points at $(0, 0, \pm\pi)$ are enforced and protected by the symmetry. Second, Dirac points can be created by the band inversion mechanism in which the sequence of bands is inverted in some regions of the momentum space. When a band inversion occurs for two doublets that have different $\widetilde{C}_{4z}$ eigenvalues, there is no hybridization between them, and a pair Dirac points can be stabilized at general points on the k_z axis.

For β'-PtO_2, the Dirac points $(0, 0, \pm k_d)$ fall into the second case. The $\widetilde{C}_{4z}$ eigenvalues of $|\psi_{\mathrm{VB}}\rangle$ are $\{\widetilde{c}_{4z}(1), \widetilde{c}_{4z}(2)\}$, and those of $|\psi_{\mathrm{CB}}\rangle$ are $\{\widetilde{c}_{4z}(0), \widetilde{c}_{4z}(3)\}$; therefore, the Dirac points can be protected even with SOC, as shown in Fig. 3(a). Besides these Dirac points near the Fermi level, we have other Dirac points, both the first and second classes, in the whole energy range that are protected by $\widetilde{C}_{4z}$. We label the bands on the k_z axis with $\widetilde{C}_{4z}$ eigenvalues in Fig. 3(b), which demonstrates the two classes of Dirac points created by the $\widetilde{C}_{4z}$ symmetry. At the zone boundary, we can observe that all points are fourfold degenerate, which is due to the nonsymmorphic nature of $\widetilde{C}_{4z}$. Additionally, on the general points on the k_z axis, the band crossing is allowed when two doublets have different $\widetilde{C}_{4z}$ eigenvalues. In this regard, β'-PtO_2 is an intriguing system with which we can simultaneously observe both classes of Dirac points.

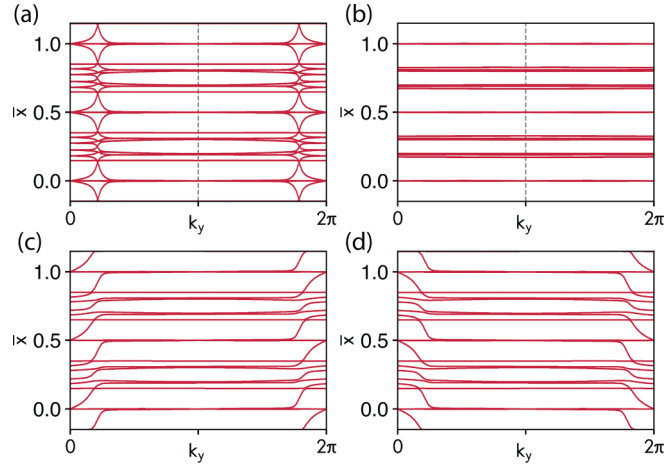

FIG. 4. Flow of the WCCs in the (a) $k_z = 0$ and (b) $k_z = \pi$ planes. They exhibit even numbers of crossings in the half Brillouin zone and therefore are $\mathbb{Z}_2$ trivial. For the $k_z = 0$ plane, the WCCs are calculated for each mirror eigensector (c) $+i$ and (d) $-i$. The Chern number of the $\pm i$ eigensector is ∓ 2, indicated by the pumping of two electrons in one period. The sign of the Chern number is determined from the propagation direction of the surface bands in Fig. 5. As a result the $k_z = 0$ plane is described by a mirror Chern number $n_M = -2$.

C. Topological properties

Having identified that β'-PtO_2 is a stable 3D DSM even with SOC, we now scrutinize the topological properties of the system. As the Dirac points are located at $k_z = \pm k_d$, the system has a full gap on the $k = 0$ and π planes. These planes can be considered 2D systems with T symmetry [39,40]; additionally, they are invariant under the M_z operation. Therefore, we can define $\mathbb{Z}_2$ invariants [41] and mirror Chern numbers [42] on the planes [6]. By calculating the flow of the Wannier charge centers (WCCs) on the $k_z = 0$ and π planes, we find that both planes are trivial in terms of the $\mathbb{Z}_2$ invariant [see Figs. 4(a) and 4(b)] [43,44]. This result can also be deduced from the same parity of $|\psi_{\mathrm{VB}}\rangle$ and $|\psi_{\mathrm{CB}}\rangle$, which are mostly composed of the d orbitals [45]. We discover, however, that the $k_z = 0$ plane has a nontrivial mirror Chern number $n_M = -2$ [see Figs. 4(c) and 4(d)], while the $k_z = \pi$ plane is trivial. The mirror Chern number $n_M = -2$ of β'-PtO_2 distinguishes it from other DSMs such as Cd_3As_2 and Na_3Bi, which carry nontrivial $\mathbb{Z}_2$ invariants. If we introduce a surface perpendicular to the mirror plane, multiple surface states corresponding to the mirror Chern number emerge at the boundary. This surface state is different from the Fermi arcs in Weyl semimetals because it is solely determined by the 2D topological invariant in the $k_z = 0$ plane.

We performed a slab calculation of β'-PtO_2 using the surface Green's function [46] constructed from the bulk's maximally localized Wannier functions [47]. We stacked unit cells along the y direction and introduced the (010) surface, whose surface band structure along the $\bar{\mathrm{M}}$-$\bar{\Gamma}$-$\bar{\mathrm{M}}$ direction is shown in Fig. 5. Depending on the surface terminations, we obtain two distinct dispersions of the surface bands. For the surface with the Pt termination [Fig. 5(a)], the surface states connect the valence band maximum and nearby conduction

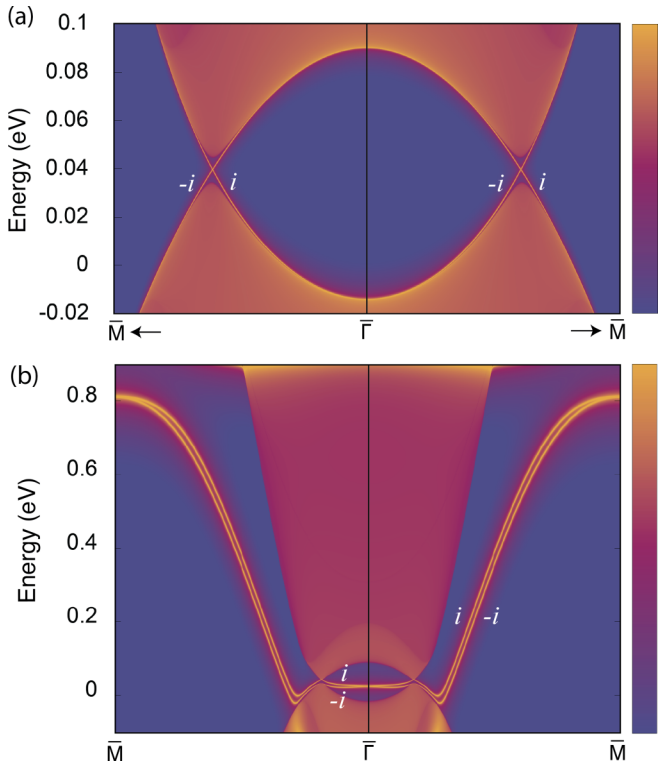

FIG. 5. Topological surface states for the (010) surfaces with (a) Pt and (b) O terminations. The warmer colors represent a higher surface contribution. Surface states are labeled by mirror eigenvalues $\pm i$. For the eigenvalue $+i$ $(-i)$, two surface states connect the valence and conduction bands from the right (left) to the left (right).

band minimum. However, for the surface with the O termination [Fig. 5(b)], the surface states connect the valence band maximum and conduction band minimum in the other half of the Brillouin zone. In either case, we observe four surface states crossing the energy gap, which are labeled with M_z eigenvalues $\pm i$ in Figs. 5(a) and 5(b). Because there are two surface states for each eigenvalue, we conclude that the $k_z = 0$ plane has a mirror Chern number $n_M = -2$. Because our calculation ignores surface potentials and complex surface configurations, the real surface states may show a different dispersion. Nevertheless, as long as the surface preserves M_z, the existence of the surface states, two surface states for each mirror eigenvalue, is guaranteed by topology. We can compare this result with the surface states of Na_3Bi [7] and Cd_3As_2 [8], which carry nontrivial $\mathbb{Z}_2$ invariants and show odd numbers of crossings in the half of the $k_z = 0$ line on the surface Brillouin zone.

The nontrivial mirror Chern number $n_M = -2$ in the $k_z = 0$ plane indicates that β'-PtO_2 can turn into a TCI by some external perturbations. Because the Dirac points $(0, 0, \pm k_d)$ are protected by the $\widetilde{C}_{4z}$ symmetry, if we break $\widetilde{C}_{4z}$ while preserving M_z, the system can become a TCI. To verify this idea, we apply a uniaxial strain along the x direction to β'-PtO_2 of the experimental lattice constants and inspect the resulting band structures. When we apply a uniaxial strain of 1%, the Dirac points are immediately gapped, as can be seen in Fig. 6(a). As the other band gaps are not opened or closed, we can identify this phase as a TCI characterized

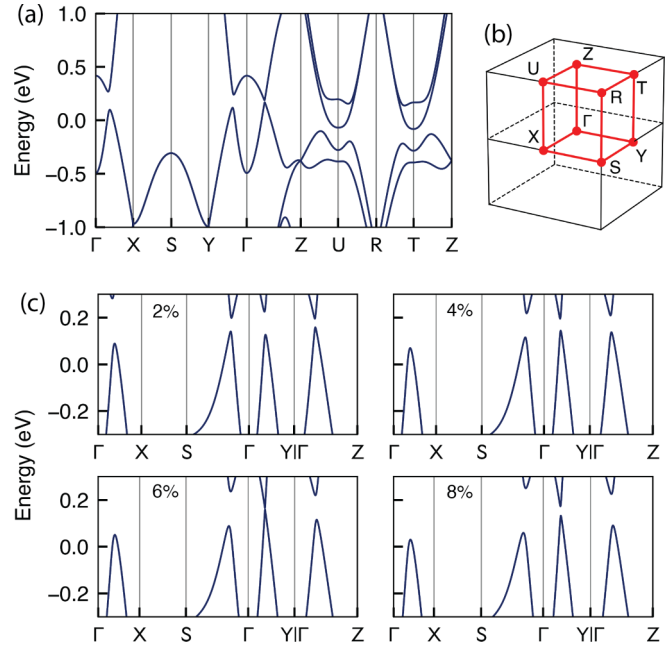

FIG. 6. (a) Band structure with uniaxial strain. A uniaxial strain of 1% along the x direction is applied to β'-PtO_2 of the experimental lattice constants. (b) Orthorhombic Brillouin zone. (c) Evolution of the band structure with uniaxial strain. The band gaps remain open until ∼6% uniaxial strain. Then, band gaps close and reopen at the points in the Γ-Y line with more strains.

by a mirror Chern number $n_M = -2$. As we increase the strain, the gapped band structure is preserved until ∼6% strain [Fig. 6(c)], which means the system maintains the TCI phase. With more strains, band gaps close and reopen at the points on the Γ-Y line, and the system undergoes a topological phase transition to a normal insulator.

D. k · p analysis

The Dirac nodal line structure and nontrivial topological invariants of β'-PtO_2 can be explained by constructing a minimal $\mathbf{k}\cdot\mathbf{p}$ Hamiltonian of the system. First, we consider the case without SOC. A general two-band Hamiltonian can be written by a 2×2 matrix, $H(\mathbf{k}) = \sum_{i=0,x,y,z} a_i(\mathbf{k})\tau_i$, where $a_i(\mathbf{k})$ is a real function of $\mathbf{k}$, τ_0 is the identity matrix, and $\tau_{x,y,z}$ are the Pauli matrices representing the orbital degree of freedom. For β'-PtO_2, by analyzing the symmetries of $|\psi_{\mathrm{VB}}\rangle$ and $|\psi_{\mathrm{CB}}\rangle$ at the Γ point, we can represent the five generators of the space group as $E = \tau_0$, $C_{2z} = \tau_0$, $\widetilde{C}_{4z} = -\tau_z$, $\widetilde{C}_{2y} = -\tau_0$, and $P = \tau_0$; in addition we can write $T = K$. With these symmetries, the Hamiltonian near the Γ point is described by the functions

$$a_x(\mathbf{k}) = v_1\left(k_x^2 - k_y^2\right),$$
$$a_y(\mathbf{k}) = 0,$$
$$a_z(\mathbf{k}) = v_2 - v_3 k_z^2 - v_4\left(k_x^2 + k_y^2\right),$$

where v_i is a constant determined by detailed electronic structures and we can neglect $a_0(\mathbf{k})$ as it does not affect the gap-closing condition. Because the energy is given by

$a_0(\mathbf{k}) \pm \sqrt{\sum_{i=x,y,z} a_i(\mathbf{k})^2}$, we solve $a_{x,y,z}(\mathbf{k}) = 0$ to obtain nodal points. By letting $k_x = \pm k_y = t/\sqrt{2}$, we obtain the solution $v_3 k_z^2 + v_4 t^2 = v_2$, which describes ellipses on the (110) and $(1\bar{1}0)$ planes consistent with the DFT results in Fig. 2(b). Including spin degree of freedom, the Hamiltonian is written by a 4×4 matrix $H(\mathbf{k}) = \sum_{i,j=0,x,y,z} a_{ij}(\mathbf{k}) \sigma_i \tau_j$, where σ_0 is the identity matrix and $\sigma_{x,y,z}$ are the Pauli matrices for spin. With SOC, we obtain the same terms as in the spinless case, i.e., $a_{0i}(\mathbf{k}) = a_i(\mathbf{k})$, but additionally, we have $a_{zy}(\mathbf{k}) = v_5 k_x k_y$, which originates from SOC. Because of this additional term, the ring-shaped nodal lines are gapped except for the two Dirac points at $k_z = \pm\sqrt{v_2/v_3}$.

The nontrivial mirror Chern number in the $k_z = 0$ plane can be explained by investigating the $\mathbf{k} \cdot \mathbf{p}$ Hamiltonian around the $(k_0, k_0, 0)$ point. We recall that this point is a Dirac point without SOC, then opens a gap when SOC is introduced. Now, we restrict the Hamiltonian to the $k_z = 0$ plane and write $H(\mathbf{k}) = H(k_x, k_y)$. To simplify the analysis, we choose $q_x = (k_x + k_y)/\sqrt{2} - \sqrt{2}k_0$ and $q_y = (-k_x + k_y)/\sqrt{2}$, which maps $(k_0, k_0) \to (0, 0)$. In the new coordinate system, the Hamiltonian including SOC is written as

$$a_{0x}(\mathbf{q}) = w_1 q_y, \; a_{0z}(\mathbf{q}) = w_2 q_x, \; a_{zy}(\mathbf{q}) = \lambda,$$

where w_1, w_2, and λ are constants [48]. Because M_z is represented by $-i\sigma_z\tau_0$, the Hamiltonian is block diagonalized into two eigensectors of M_z. For the $\pm i$ eigensectors, the Hamiltonian is written by a 2×2 matrix, $H_{\pm i}(\mathbf{q}) = \mathbf{a}_{\pm i}(\mathbf{q}) \cdot \boldsymbol{\tau}$, where $\mathbf{a}_{\pm i}(\mathbf{q}) = (w_1 q_y, \mp\lambda, w_2 q_x)$, which describes massive Dirac fermions with the mass term λ. The Chern number of the Hamiltonian is explicitly calculated, which gives $-\frac{1}{2}\,\mathrm{sgn}(w_1 w_2 \lambda)$ for the $+i$ eigensector. Since there are four Dirac points without SOC that are related by the $\widetilde{C}_{4z}$ symmetry, they together give a Chern number $n_i = -2\,\mathrm{sgn}(w_1 w_2 \lambda)$ when SOC opens the gaps. However, for the $-i$ eigensector, the Chern number has the opposite sign because the mass term flips the sign. Consequently, we classify the $k_z = 0$ plane as a TCI with a mirror Chern number of $|2|$, whose sign should be fixed by the detailed electronic structure. This nontrivial topological invariant is consistent with the flow of WCCs [Figs. 4(c) and 4(d)] and the surface band calculations [Fig. 5].

IV. DISCUSSION AND SUMMARY

We have so far showed that β'-PtO_2 is a topological DSM that possesses a nontrivial mirror Chern number $n_M = -2$. At this point, it is appropriate to address the shortcomings of the GGA calculations because the correct description of band positions is crucial when Dirac points are created by the band inversion mechanism. As there are no experimental data regarding the band structure of β'-PtO_2, we have to rely on the first-principles calculations at this moment. Considering the well-known band gap underestimation of the GGA calculations, we need to verify whether the DSM phase of β'-PtO_2 is retained when we use a higher-level exchange-correlation functional. For this purpose, we employ the HSE functional, in which an amount of exact exchange energy, determined by a mixing parameter α, is added to the exchange-correlation energy of the GGA.

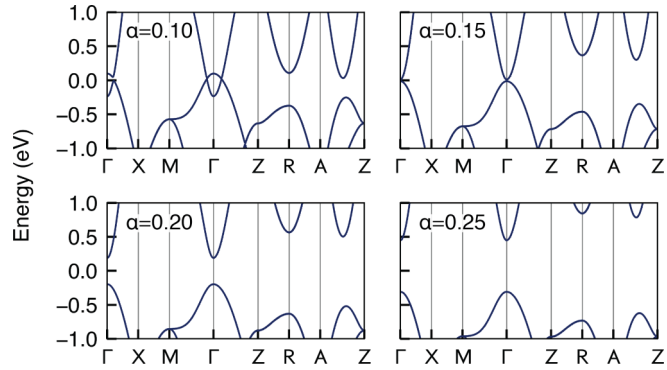

FIG. 7. HSE band structures with mixing parameter $\alpha = 0.10$, 0.15, 0.20, and 0.25. The band gap increases as α increases. For $\alpha = 0.1$ to 0.15, which is more appropriate for the transition-metal systems than $\alpha = 0.25$ [49–52], an ideal DSM phase is observed.

We show the HSE band structures of β'-PtO_2 with the experimental lattice constants in Fig. 7. Compared with the GGA band structure in Fig. 1(c), the band gap is significantly increased in the HSE calculations. For $\alpha = 0.10$, 0.15, 0.20, and 0.25, the band gaps at the Γ point are −0.33, 0.025, 0.39, and 0.76 eV, respectively. Although $\alpha = 0.25$ is widely used, we emphasize that there is no universal mixing parameter that provides a good description for all materials. Especially for rutile and perovskite oxides with transition-metal ions, it is known that the smaller mixing parameters $\alpha = 0.1$ to 0.15 are more appropriate than the value $\alpha = 0.25$ [49–52]. When the mixing parameter is from 0.1 to 0.15, the band structure of β'-PtO_2 exhibits an ideal 3D DSM phase, where only the Dirac points are pinned at the Fermi level [Fig. 7]. Based on these observations, we hope future experiments will confirm the DSM phase of β'-PtO_2.

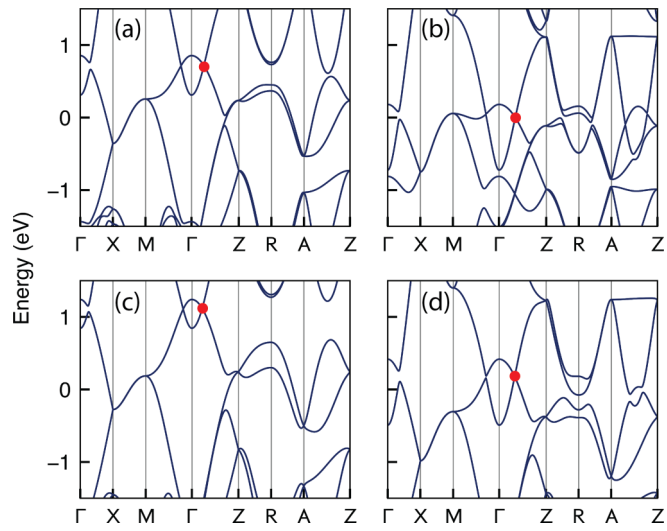

FIG. 8. GGA + SOC band structures of (a) RhO_2 ($a = 4.487$ Å, $c = 3.089$ Å [53]), (b) PdO_2 ($a = 4.483$ Å, $c = 3.101$ Å [54]), and (c) IrO_2 ($a = 4.505$ Å, $c = 3.159$ Å [55]). (d) The band structure of β'-PtO_2 ($a = 4.485$ Å, $c = 3.130$ Å [32]) is redrawn for comparison. Red dots denote Dirac points.

Besides β'-PtO_2, possible candidates for 3D topological DSMs include rutile phase RhO_2, PdO_2, and IrO_2, whose GGA + SOC band structures are shown in Fig. 8. They share similar band structures, but RhO_2 and IrO_2 need one electron doping per formula unit because we require six electrons in the d orbitals to pin the Dirac points to the Fermi level. Although such a high level of doping seems impossible, it was recently reported that the rutile structure VO_2 can be doped with one electron by using hydrogen atoms [56]; therefore, we expect that similar experiments could be possible for RhO_2 and IrO_2.

In summary, we have theoretically identified the crystalline topological DSM phase in the transition-metal rutile oxides as illustrated by β'-PtO_2. The Dirac points on the k_z axis are protected by the fourfold screw rotation $\tilde{C}_{4z}$ in this class of materials. Distinct from the known Dirac semimetals such as Cd_3As_2 and Na_3Bi, the topological properties of the system are characterized by the nontrivial mirror Chern number $n_M = -2$ on the $k_z = 0$ plane. It indicates that a distortion, which breaks the $\tilde{C}_{4z}$ symmetry and preserves the M_z symmetry, can make a TCI phase in the system. Our proposal is likely to lead to a topologically nontrivial DSM phase with strong correlation since the observation is universal among transition-metal rutile oxides with six electrons in the d orbitals.

ACKNOWLEDGMENTS

This work was supported by the Institute for Basic Science (IBS) in Korea (Grant No. IBS-R009-D1). B.-J.Y. was also supported by the Basic Science Research Program through the National Research Foundation of Korea (NRF; Grants No. 0426-20170012, and No. 0426-20180011), the POSCO Science Fellowship of the POSCO TJ Park Foundation (No. 0426-20180002), and the U.S. Army Research Office under Grant No. W911NF-18-1-0137.

[1] S.-Y. Xu, I. Belopolski, N. Alidoust, M. Neupane, G. Bian, C. Zhang, R. Sankar, G. Chang, Z. Yuan, C.-C. Lee, S.-M. Huang, H. Zheng, J. Ma, D. S. Sanchez, B. Wang, A. Bansil, F. Chou, P. P. Shibayev, H. Lin, S. Jia, and M. Z. Hasan, Discovery of a Weyl fermion semimetal and topological Fermi arcs, Science **349**, 613 (2015).

[2] T. Liang, Q. Gibson, M. N. Ali, M. Liu, R. J. Cava, and N. P. Ong, Ultrahigh mobility and giant magnetoresistance in the Dirac semimetal Cd_3As_2, Nat. Mater. **14**, 280 (2015).

[3] P. J. W. Moll, N. L. Nair, T. Helm, A. C. Potter, I. Kimchi, A. Vishwanath, and J. G. Analytis, Transport evidence for Fermi-arc-mediated chirality transfer in the Dirac semimetal Cd_3As_2, Nature (London) **535**, 266 (2016).

[4] Y. Kim, B. J. Wieder, C. L. Kane, and A. M. Rappe, Dirac Line Nodes in Inversion-Symmetric Crystals, Phys. Rev. Lett. **115**, 036806 (2015).

[5] R. Yu, H. Weng, Z. Fang, X. Dai, and X. Hu, Topological Node-Line Semimetal and Dirac Semimetal State in Antiperovskite Cu_3PdN, Phys. Rev. Lett. **115**, 036807 (2015).

[6] B.-J. Yang and N. Nagaosa, Classification of stable three-dimensional Dirac semimetals with nontrivial topology, Nat. Commun. **5**, 4898 (2014).

[7] Z. Wang, Y. Sun, X.-Q. Chen, C. Franchini, G. Xu, H. Weng, X. Dai, and Z. Fang, Dirac semimetal and topological phase transitions in A_3Bi (A = Na, K, Rb), Phys. Rev. B **85**, 195320 (2012).

[8] Z. Wang, H. Weng, Q. Wu, X. Dai, and Z. Fang, Three-dimensional Dirac semimetal and quantum transport in Cd_3As_2, Phys. Rev. B **88**, 125427 (2013).

[9] S. M. Young, S. Zaheer, J. C. Y. Teo, C. L. Kane, E. J. Mele, and A. M. Rappe, Dirac Semimetal in Three Dimensions, Phys. Rev. Lett. **108**, 140405 (2012).

[10] J. A. Steinberg, S. M. Young, S. Zaheer, C. L. Kane, E. J. Mele, and A. M. Rappe, Bulk Dirac Points in Distorted Spinels, Phys. Rev. Lett. **112**, 036403 (2014).

[11] Z. K. Liu, B. Zhou, Y. Zhang, Z. J. Wang, H. M. Weng, D. Prabhakaran, S. K. Mo, Z. X. Shen, Z. Fang, X. Dai, Z. Hussain, and Y. L. Chen, Discovery of a three-dimensional topological Dirac semimetal, Na_3Bi, Science **343**, 864 (2014).

[12] M. Neupane, S.-Y. Xu, R. Sankar, N. Alidoust, G. Bian, C. Liu, I. Belopolski, T.-R. Chang, H.-T. Jeng, H. Lin, A. Bansil, F. Chou, and M. Z. Hasan, Observation of a three-dimensional topological Dirac semimetal phase in high-mobility Cd_3As_2, Nat. Commun. **5**, 386 (2014).

[13] Z. K. Liu, J. Jiang, B. Zhou, Z. J. Wang, Y. Zhang, H. M. Weng, D. Prabhakaran, S. K. Mo, H. Peng, P. Dudin, T. Kim, M. Hoesch, Z. Fang, X. Dai, Z. X. Shen, D. L. Feng, Z. Hussain, and Y. L. Chen, A stable three-dimensional topological Dirac semimetal Cd_3As_2, Nat. Mater. **13**, 677 (2014).

[14] S. Jeon, B. B. Zhou, A. Gyenis, B. E. Feldman, I. Kimchi, A. C. Potter, Q. D. Gibson, R. J. Cava, A. Vishwanath, and A. Yazdani, Landau quantization and quasiparticle interference in the three-dimensional Dirac semimetal Cd_3As_2, Nat. Mater. **13**, 851 (2014).

[15] T.-R. Chang, S.-Y. Xu, D. S. Sanchez, W.-F. Tsai, S.-M. Huang, G. Chang, C.-H. Hsu, G. Bian, I. Belopolski, Z.-M. Yu, S. A. Yang, T. Neupert, H.-T. Jeng, H. Lin, and M. Z. Hasan, Type-II Symmetry-Protected Topological Dirac Semimetals, Phys. Rev. Lett. **119**, 026404 (2017).

[16] A. A. Soluyanov, B. A. Bernevig, D. Gresch, M. Troyer, Q. Wu, X. Dai, and Z. Wang, Type-II Weyl semimetals, Nature (London) **527**, 495 (2015).

[17] H. Huang, Z. Liu, H. Zhang, W. Duan, and D. Vanderbilt, Emergence of a Chern-insulating state from a semi-Dirac dispersion, Phys. Rev. B **92**, 161115 (2015).

[18] J. L. Lado, D. Guterding, P. Barone, R. Valentí, and V. Pardo, Quantum spin Hall effect in rutile-based oxide multilayers, Phys. Rev. B **94**, 235111 (2016).

[19] Y. Sun, Y. Zhang, C.-X. Liu, C. Felser, and B. Yan, Dirac nodal lines and induced spin Hall effect in metallic rutile oxides, Phys. Rev. B **95**, 235104 (2017).

[20] Z. Wang and G. Wang, A new strongly topological node-line semimetal β-PbO_2, Phys. Lett. A **381**, 2856 (2017).

[21] W. Wang, L. Deng, N. Jiao, P. Zhou, and L. Sun, Three-dimensional Dirac semimetal β-PbO_2, Phys. Status Solidi RRL **11**, 1700271 (2017).

[22] A. Sekine and K. Nomura, Stability of multinode Dirac semimetals against strong long-range correlations, Phys. Rev. B **90**, 075137 (2014).

[23] B. Roy, P. Goswami, and V. Juričić, Interacting Weyl fermions: Phases, phase transitions, and global phase diagram, Phys. Rev. B **95**, 201102(R) (2017).

[24] S. E. Han and E.-G. Moon, Long-range Coulomb interaction effects on the topological phase transitions between semimetals and insulators, Phys. Rev. B **97**, 241101(R) (2018).

[25] P. Goswami and S. Chakravarty, Quantum Criticality Between Topological and Band Insulators in $3+1$ Dimensions, Phys. Rev. Lett. **107**, 196803 (2011).

[26] P. Hosur, S. A. Parameswaran, and A. Vishwanath, Charge Transport in Weyl Semimetals, Phys. Rev. Lett. **108**, 046602 (2012).

[27] G. Li, B. Yan, Z. Wang, and K. Held, Topological Dirac semimetal phase in Pd and Pt oxides, Phys. Rev. B **95**, 035102 (2017).

[28] G. Kresse and J. Furthmüller, Efficient iterative schemes for *ab initio* total-energy calculations using a plane-wave basis set, Phys. Rev. B **54**, 11169 (1996).

[29] P. E. Blöchl, Projector augmented-wave method, Phys. Rev. B **50**, 17953 (1994).

[30] J. P. Perdew, K. Burke, and M. Ernzerhof, Generalized Gradient Approximation Made Simple, Phys. Rev. Lett. **77**, 3865 (1996).

[31] J. Heyd, G. E. Scuseria, and M. Ernzerhof, Hybrid functionals based on a screened Coulomb potential, J. Chem. Phys. **118**, 8207 (2003).

[32] M. P. H. Fernandez and B. L. Chamberland, A new high pressure form of PtO_2, J. Less-Common Met. **99**, 99 (1984).

[33] R. D. Shannon, Synthesis and properties of two new members of the rutile family RhO_2 and PtO_2, Solid State Commun. **6**, 139 (1968).

[34] A. N. Mansour, D. E. Sayers, J. W. Cook, D. R. Short, R. D. Shannon, and J. R. Katzer, X-ray absorption studies of some platinum oxides, J. Phys. Chem. **88**, 1778 (1984).

[35] R. K. Nomiyama, M. J. Piotrowski, and J. L. F. Da Silva, Bulk structures of PtO and PtO_2 from density functional calculations, Phys. Rev. B **84**, 100101 (2011).

[36] T. Bzdušek, Q. Wu, A. Rüegg, M. Sigrist, and A. A. Soluyanov, Nodal-chain metals, Nature (London) **538**, 75 (2016).

[37] G. Chang, S.-Y. Xu, X. Zhou, S.-M. Huang, B. Singh, B. Wang, I. Belopolski, J. Yin, S. Zhang, A. Bansil, H. Lin, and M. Z. Hasan, Topological Hopf and Chain Link Semimetal States and Their Application to Co_2MnGa, Phys. Rev. Lett. **119**, 156401 (2017).

[38] B.-J. Yang, T. Morimoto, and A. Furusaki, Topological charges of three-dimensional Dirac semimetals with rotation symmetry, Phys. Rev. B **92**, 165120 (2015).

[39] J. E. Moore and L. Balents, Topological invariants of time-reversal-invariant band structures, Phys. Rev. B **75**, 121306(R) (2007).

[40] L. Fu, C. L. Kane, and E. J. Mele, Topological Insulators in Three Dimensions, Phys. Rev. Lett. **98**, 106803 (2007).

[41] C. L. Kane and E. J. Mele, Z_2 Topological Order and the Quantum Spin Hall Effect, Phys. Rev. Lett. **95**, 146802 (2005).

[42] J. C. Y. Teo, L. Fu, and C. L. Kane, Surface states and topological invariants in three-dimensional topological insulators: Application to $Bi_{1-x}Sb_x$, Phys. Rev. B **78**, 045426 (2008).

[43] A. A. Soluyanov and D. Vanderbilt, Wannier representation of $\mathbb{Z}_2$ topological insulators, Phys. Rev. B **83**, 035108 (2011).

[44] R. Yu, X.-L. Qi, A. Bernevig, Z. Fang, and X. Dai, Equivalent expression of $\mathbb{Z}_2$ topological invariant for band insulators using the non-Abelian Berry connection, Phys. Rev. B **84**, 075119 (2011).

[45] L. Fu and C. L. Kane, Topological insulators with inversion symmetry, Phys. Rev. B **76**, 045302 (2007).

[46] M. P. L. Sancho, J. M. L. Sancho, and J. Rubio, Highly convergent schemes for the calculation of bulk and surface Green functions, J. Phys. F **15**, 851 (1985).

[47] A. A. Mostofi, J. R. Yates, Y.-S. Lee, I. Souza, D. Vanderbilt, and N. Marzari, `wannier90`: A tool for obtaining maximally-localised Wannier functions, Comput. Phys. Commun. **178**, 685 (2008).

[48] If we include higher-order terms, we have $a_{0x}(q_x, q_y) = w_1 q_y + w_3 q_x q_y$ and $a_{0z}(q_x, q_y) = w_2 q_x + w_4 q_x^2 + w_5 q_y^2$. This is the same form as the type-II semi-Dirac dispersion introduced in Ref. [17]. We note that the linear term is the most important one for the nontrivial Chern number.

[49] J. P. Perdew, M. Ernzerhof, and K. Burke, Rationale for mixing exact exchange with density functional approximations, J. Chem. Phys. **105**, 9982 (1996).

[50] J. E. Coulter, E. Manousakis, and A. Gali, Limitations of the hybrid functional approach to electronic structure of transition metal oxides, Phys. Rev. B **88**, 041107 (2013).

[51] J. He and C. Franchini, Screened hybrid functional applied to $3d^0 \rightarrow 3d^8$ transition-metal perovskites $LaMO_3$ (M = Sc–Cu): Influence of the exchange mixing parameter on the structural, electronic, and magnetic properties, Phys. Rev. B **86**, 235117 (2012).

[52] C. Franchini, Hybrid functionals applied to perovskites, J. Phys.: Condens. Matter **26**, 253202 (2014).

[53] G. Demazeau, A. Baranov, R. Pöttgen, L. Kienle, M. H. Möller, R.-D. Hoffmann, and M. Valldor, An anhydrous high-pressure synthesis route to rutile type RhO_2, Z. Naturforsch. B **61**, 1500 (2006).

[54] I. S. Shaplygin, G. L. Aparnikov, and V. B. Lazarev, Preparation of palladium dioxide at high pressure, Zh. Neorg. Khim. **23**, 884 (1978).

[55] A. A. Bolzan, C. Fong, B. J. Kennedy, and C. J. Howard, Structural studies of rutile-type metal dioxides, Acta Crystallogr., Sect. B **53**, 373 (1997).

[56] H. Yoon, M. Choi, T.-W. Lim, H. Kwon, K. Ihm, J. K. Kim, S.-Y. Choi, and J. Son, Reversible phase modulation and hydrogen storage in multivalent VO_2 epitaxial thin films, Nat. Mater. **15**, 1113 (2016).